# Chapter 5
# Collective Instabilities in the Tevatron Collider Run II Accelerators

**A. Burov, V. Lebedev, L. Prost, A. Shemyakin, V. Shiltsev, J. Steimel, and C.Y. Tan**

## 5.1 Phenomenology of Beam Instabilities in the Tevatron Complex

High luminosity operation of the Tevatron during Collider Run II required high beam intensities all over the accelerator complex, and as a result, five out of six rings (except the Debuncher) had notable problems with beam stability. The instabilities of almost every type were present there: single and multibunch, transverse and longitudinal, due to electromagnetic interaction with vacuum chamber and due to interaction with ions stored in the beam, instabilities happened in both proton and antiproton beams. In many cases, various methods to suppress the instabilities have been implemented, including various damping systems—see Table 5.1. The most severe issues with serious impact on operations were related to transverse head-tail instability in the Tevatron, transverse beam instability in the Booster, instabilities in the Recycler antiproton beams, and longitudinal instabilities in the Tevatron.

### *5.1.1 Transverse Head-Tail Instability in the Tevatron*

Transverse bunch weak head-tail instability was a serious limitation on the maximum bunch current in the Tevatron [1]. It manifested itself as a very fast (50–100 turns) development of vertical or horizontal oscillations and consequent beam loss on the aperture—see Fig. 5.1—accompanied by simultaneous emittance blowup of many bunches in the bunch train. For a long time, the only way to stabilize it was to

A. Burov • V. Lebedev (✉) • L. Prost • A. Shemyakin • V. Shiltsev (✉) • J. Steimel • C.Y. Tan
Fermi National Accelerator Laboratory, PO Box 500, Batavia, IL 60510, USA
e-mail: val@fnal.gov; shiltsev@fnal.gov

V. Lebedev and V. Shiltsev (eds.), *Accelerator Physics at the Tevatron Collider*, Particle Acceleration and Detection, DOI 10.1007/978-1-4939-0885-1_5,

**Table 5.1** Instabilities and cures in the Tevatron Run II accelerators

| | Instability nature | | Dampers | |
|---|---|---|---|---|
| | Longitudinal | Transverse | Longitudinal | Transverse |
| Booster | Multibunch, cavities | Laminated wall, space charge | Narrow band | – |
| Main injector | Multibunch | Multibunch | Bunch by bunch | Bunch by bunch |
| Accumulator | Stochastic cooling | Due to stores ions | – | Wideband |
| Recycler | – | Head-tail, resistive wall | – | Wideband |
| Tevatron | "Bunch dancing" | Head-tail, resistive wall | Bunch by bunch, protons only | Bunch by bunch, protons only |

operate Tevatron with high linear chromaticity in both planes $Q'_{x,y} > 10$. High chromaticity values led to short beam lifetime especially in the presence of opposite beam (see Sect. 8.2).

Transverse bunch-by-bunch dampers (vertical and horizontal) were built and commissioned in 2002–2003 [2] and allowed to keep the beam stable at lower chromaticities at the injection energy of 150 GeV (see table below).

| | | |
|---|---|---|
| Originally | 2002 | $Q' \sim 10$–16 |
| V/H dampers installed | 2003 | $Q' \sim 5$–8 |
| Lambertsons liner | 2004 | $Q' \sim 3$–5 |
| V-damper fights H-damper | Dec 2004 | $Q' \sim 8$–10 |
| Octupoles commissioned | Feb 2005 | $Q' \sim 0$–3 |

As seen from the above, other less operationally challenging methods were later employed to secure the beam stability, namely, (a) 0.4 mm thin conductive CuBe liners being installed inside Lambertson magnets that reduced the total Tevatron transverse impedance from $Z_\perp \approx 5$–2.4 MOhm/m to about 1 MOhm/m [1] and (b) commissioning of new circuits of octupoles [3] which generated additional tune spread in the beams and eventually allowed the reduction of chromaticity to a few (0–3) units at 150 GeV and improved beam lifetime to better than 20 h. In December 2004, it was observed that vertical and horizontal dampers "fought" each other—so, one of them had to be turned off (and correspondingly, $Q'$ in that plane had to be increased) in order to let the other one work. A lot of effort was put into investigation of the phenomena—the leading hypothesis was that it is due to local coupling—but there was no satisfactory resolution. So, as soon as the new octupole circuits were operational, the dampers were disabled.

### *5.1.2 Coherent Synchro-betatron Resonance in the Booster*

Booster is a fast cycling proton synchrotron operating at 15 Hz. To exclude the eddy currents excited in the vacuum chamber by fast changing magnetic field,

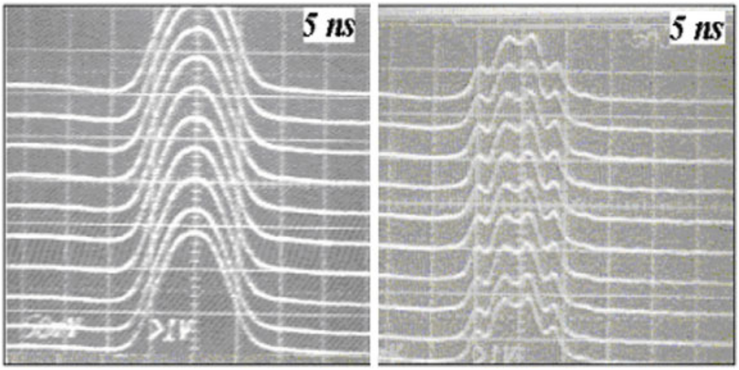


**Fig. 5.1** Oscilloscope traces of the longitudinal density profiles of (**a**) the initial ($N_p = 2.6 \times 10^{11}$) and (**b**) remaining ($N_p = 2.6 \times 10^{11}$) 150 GeV proton bunches before and after vertical $l = 2$ weak head-tail instability [1]

its vacuum chamber is formed by poles of laminated combined function dipoles. That addresses the problems related to the eddy currents but greatly contributes to the transverse and longitudinal impedances. In particular, the transverse impedances achieve values of about 100 MΩ/m (see details in Sect. 5.2) adversely affecting beam stability. In operation, the instabilities are suppressed by large chromaticities, $Q'_{x,y} \sim 10\text{–}16$. That results in deterioration of the dynamic aperture and the beam lifetime. Our attempts to stabilize the instability with transverse feedback system carried out before and in the course of Tevatron Run II were unsuccessful.

The first detailed studies of beam stability were carried out in 2005 and were mostly devoted to the beam stability at the injection energy [4]. They exhibited that at reduced chromaticity the head-tail motion develops extremely fast with growth time of about 12 turns at nominal Booster intensity and about 14 turns at the half of nominal intensity. For both cases the fractional part of head-tail betatron frequency was close to zero.

Figure 5.2 presents parameters of bunches for the first 150 turns after injection starts at the nominal beam intensity. The process looks as following. First, an injection orbit bump is created just before the injection. Then, the linac beam is injected over several turns (1–11). When the injection is finished the orbit bump is switched off (it takes 10–20 turns) and RF voltage is adiabatically increased causing the beam to be bunched at turn 70 with RF voltage continuing to grow. The first sign of the instability appears at turn 80 causing the beam intensity drop after turn 100. The results of the measurements [4] demonstrated that the instability develops only after bunches are formed, and that its growth rate is weakly dependent on the beam intensity. Later analysis [5] showed that the observed behavior corresponds to the coherent synchro-betatron resonance which develops when the synchro-betatron tune is close to an integer: $Q_{x,y} + 3Q_s \approx 7$. Note the synchrotron tune at injection is quite high $Q_s \approx 0.07$ and the resonance happens even if working tunes are quite

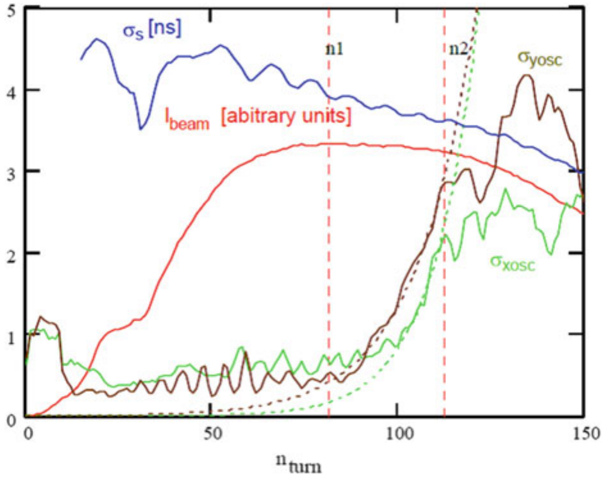


**Fig. 5.2** Changes of beam parameters during first 150 turns after injection in the Booster; *red line* AC beam intensity, *blue line* rms bunch length, *vertical* (*brown line*) and *horizontal* (*green line*) rms transverse dipole moments. *Dotted lines* present exponential fits to the rms dipole moments inside a bunch. All signals are averaged over all 84 bunches; total proton intensity is $4.5 \cdot 10^{12}$ [4]

far from the integer resonance. Large value of incoherent betatron tune shift due to space charge tune ($\delta Q_{SC} \approx -0.35$) pushes the bare tunes being above 6.85 making impossible to avoid the resonance in the course of adiabatic bunching. The variation of the growth time from 18 to 12 turns for intensity variation in the range [1–5] . $10^{12}$ protons per beam is related to the interference between the synchro-betatron coherent resonance and the head-tail multi-bunch instability related to the large transverse impedance. In the absence of the synchro-betatron resonance, the instability growth time in vicinity of injection energy and small chromaticity is about 100 turns.

### 5.1.3 Transverse Instability in High-Brightness Antiproton Beam in Recycler

The Recycler ring (RR) is the last (third) ring in a chain of antiproton cooling and stacking stages. Transverse instabilities in RR have been theoretically studied during its design but were deemed a marginal issue for the maximum number of antiprotons that were expected to be stored at any time ($<250 \times 10^{10}$). With strong electron cooling and up to $5 \times 10^{12}$ stored antiprotons, much brighter beams than initially anticipated are generated. As a result, emittances of the cooled beam are limited by a transverse resistive wall instability. (An ion-capture-driven instability was identified very early in the Recycler operation and was eliminated with clearing

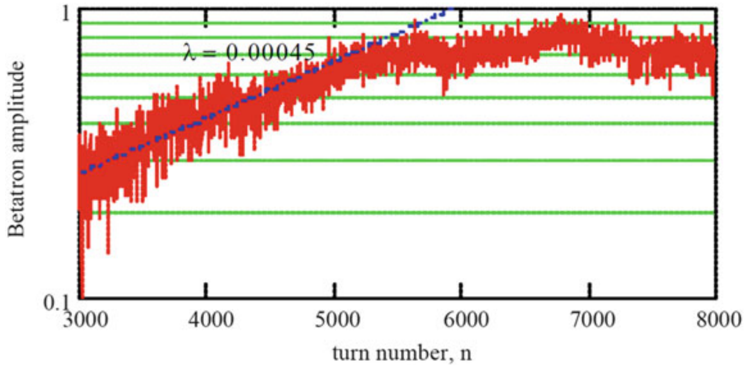


**Fig. 5.3** Growth of the betatron oscillations in high-brightness antiproton beam in Recycler without dampers [8]

electrodes and the fact that the stored beam was bunched.) A damper system was installed in 2005 with an initial bandwidth of 30 MHz and eventually upgraded to 70 MHz. Nevertheless, several instabilities were observed during normal operation and prompted studies to better understand their nature and characteristics, as well as to limit their occurrences [6].

A typical instability is characterized by three phenomena: a large and sharp increase of the damper kickers' amplitudes (in particular, the vertical damper kicker), a fast increase of the emittances (mostly vertical) as measured by the Schottky detectors, and a relatively slow beam loss. The instability lasts for 5–15 s, and accordingly, the beam loss is slow. The antiproton emittances measured by the flying wires are almost unaffected by the instability, thus, indicating that this is mostly the tail particles that suffer from the instability and are being lost to the aperture. That observation is also consistent with the general picture of the Landau damping [7]. Without the dampers (or with malfunctioning dampers), most of the beam loss and the emittance blowup happen in $<0.1$ s (see Fig. 5.3). There is very little motion in the head of a ~6 μs bunch and maximum oscillations occur in the trailing half of the bunch (at some ~2/3 of the bunch length).

To support high luminosity operation of the collider complex, the highest possible effective phase density $D_{95}$ of antiprotons is required. It is defined as

$$D_{95} = \frac{N_a}{4\varepsilon_L 6\varepsilon_T}, \tag{5.1}$$

where $N_a$ is the total number of antiprotons in the Recycler (in the units of $10^{10}$), $\varepsilon_L$ is the rms longitudinal emittance (in $\text{eV} \cdot \text{s}$), and $\varepsilon_T$ is the rms normalized transverse emittance (in μm). The numerical factors are chosen to simplify calculations for widely used "95 % emittance" values for the Gaussian distributions. Without

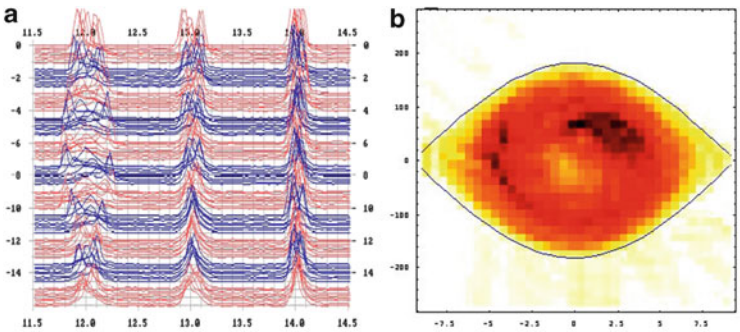

**Fig. 5.4** (**a**) "Waterfall" plot of three "dancing" uncoalesced bunches of 150 GeV protons some 19 ns apart; (**b**) tomography of the longitudinal phase space of a high intensity proton bunch in the Tevatron [9]

feedback systems, the operationally achievable factor was limited to $D_{95} < 1.0$, while it did reach as high as 2.6 with 30 MHz bandwidth damper and up to $D_{95} \approx 4.4$ after commissioning of the 70 MHz bandwidth damper system [6].

### *5.1.4 Longitudinal Instabilities in the Tevatron*

The phenomenon of "dancing bunches" in Tevatron refers to notable longitudinal single bunch and coupled bunch instabilities in the proton beam [9, 10]. At the Tevatron injection energy of 150 GeV, large (up to 1 rad) RF beam phase oscillations in high intensity beams can persist for many minutes (see Fig. 5.4, [9]).

The biggest concern for operations was that the "dancing bunches" result in slow bunched beam intensity loss and increase of the "DC beam" intensity (uncaptured particles out of sync with the RF system) which is lost at the start of acceleration. Another manifestation was the regular occurrence of large longitudinal bunch oscillations at 980 GeV energy accompanied by significant longitudinal emittance increase, reduction of luminosity, beam losses, and accumulation of particles in the abort gaps—all of which are very dangerous for operations (see Fig. 5.5). To counteract that, a longitudinal bunch-by-bunch damper was designed, built, installed, and commissioned in the Tevatron in 2002 [11]. Since then, the damper is in operation for every store all the times except the energy ramp. It effectively suppresses both the "dancing bunches" and the single and coupled bunch instabilities. It was found that to be effective, the damper gain should vary slowly during the store in a fashion which tracks proton bunch intensity and bunch length gain $\sim N/\sigma_z$. Unfortunately, from time to time, the instability still occurred. The cause of these outbreaks of the instability has not been fully understood. At the later years of the Collider Run II, similar phenomena started to appear in high intensity antiproton beam as well, corresponding damper system has been installed but has not been commissioned due to lack of time.

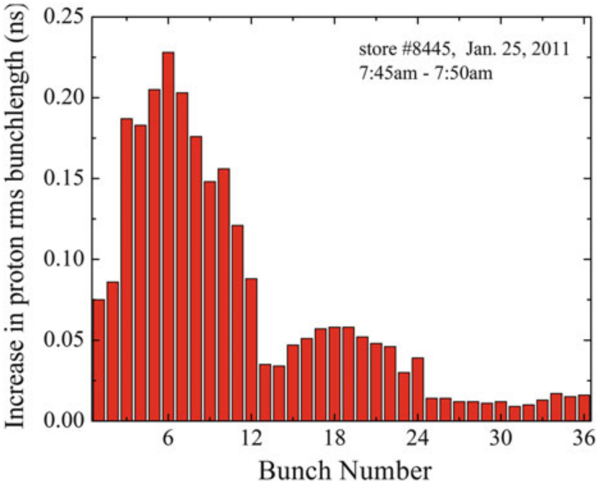


**Fig. 5.5** Increase in the rms length of individual proton bunched during the occurrence of longitudinal instability over the course of the HEP store #8445 (from 7:45 am to 7:50 am on January 25, 2011). Before the blowup, the rms bunch length of all the bunches was $2.04 \pm 0.03$ ns

## 5.2 Impedances of Laminated Vacuum Chambers

Below, the longitudinal and transverse impedances are derived for round and flat laminated vacuum chambers, and results applied to the Fermilab Booster.

First publications on impedance of laminated vacuum chambers are related to the early 1970s: those are of S.C. Snowdon [12] and of A.G. Ruggiero [13]; 15 years later, a revision paper of R. Gluckstern appeared [14]. All the publications were presented as Fermilab preprints, and that is of no surprise as the Fermilab Booster has its laminated magnets open to the beam. Being in a reasonable mutual agreement, these publications were all devoted to the longitudinal impedance of round vacuum chambers. The transverse impedance and the flat geometry case were addressed in more recent paper of K.Y. Ng [15]. The latest computer calculations of A. Macridin et al. [16] revealed some disagreement with [15] that stimulated further theoretical investigation presented below, which ended up with results in agreement with [16].

Some general conditions are assumed here. First, the frequencies under interest, $\omega$, are supposed to be sufficiently low [17, 18]:

$$\begin{aligned} &\omega << \gamma\beta c/a \\ &\omega << 4\pi\sigma/\varepsilon \end{aligned} \tag{5.2}$$

where $a$ is the aperture radius, $\gamma$ and $\beta$ are the relativistic factors, $c$ is the speed of light, and $\sigma$ and $\varepsilon$ are the chamber conductivity and dielectric constant. The first condition actually requires the wavelength of the fields to be much longer than the aperture, as they are seen in the beam frame. Note that the specified wavelength parameter $\gamma\beta c/(a\omega)$ is relevant to the wake forces, not to the electric and magnetic fields taken separately. For the separate field components, the relativistic factor does not count; but it does count for the wakes (see, e.g., [19], Eq. (2.41)).

The above condition seems to be satisfied for all practically interesting cases. It allows one to neglect the longitudinal magnetic field, and consequently, the transverse components of the vector potential vanish. The second condition means that the beam electric moments are shielded infinitesimally fast at the chamber surface. While this condition is well satisfied for metals, it may be violated for ferrites [20]. The last case is irrelevant to this chapter, since the laminations are metallic (iron). We also imply that the laminations are thin: $h,d << a$ and that the skin depth, $\delta$, is much smaller than the lamination thickness, $d$.

### 5.2.1 Flat Chamber: Longitudinal Impedance

Let the beam current be modulated at a frequency $\omega$:

$$I(\mathbf{r},t) = I_0\delta(\mathbf{r}_\perp)\exp(-i\omega(t - z/v)). \tag{5.3}$$

Due to the horizontal homogeneity, the problem can be solved by the Fourier transform over this coordinate

$$F(x) = \int_{-\infty}^{\infty} F_k \exp(ik_x x)\frac{dk_x}{2\pi}. \tag{5.4}$$

Since only the Fourier components are used below, the subscript $k$ can be safely omitted. For long wavelength, the vector potential reduces to its longitudinal component only. In the free space, it satisfies the transverse Laplace equation and can be presented as

$$A = \frac{I_0 Z_0}{2k_x}\left[\exp(-k_x y) - G\frac{\cosh(k_x y)}{\cosh(k_x a)}\exp(-k_x a)\right]; \quad k_x > 0, \quad 0 < y < a, \tag{5.5}$$

where $Z_0 = 4\pi/c = 377\,\Omega$, $a$ is the half gap (see Fig. 5.6), $G = G(k_x)$ is the function to be determined from the boundary conditions, and the vector potential is an even function of $k_x$ and $y$. The first term inside the square brackets describes a direct field of the beam, while the second one is the response due to the induced currents. From here, a ratio of the magnetic fields follows:

$$\left.\frac{H_y}{H_x}\right|_{y=a-0} = i\frac{1 - G}{1 + G\tanh(k_x a)}. \tag{5.6}$$

**Fig. 5.6** Geometry of the laminated vacuum chamber

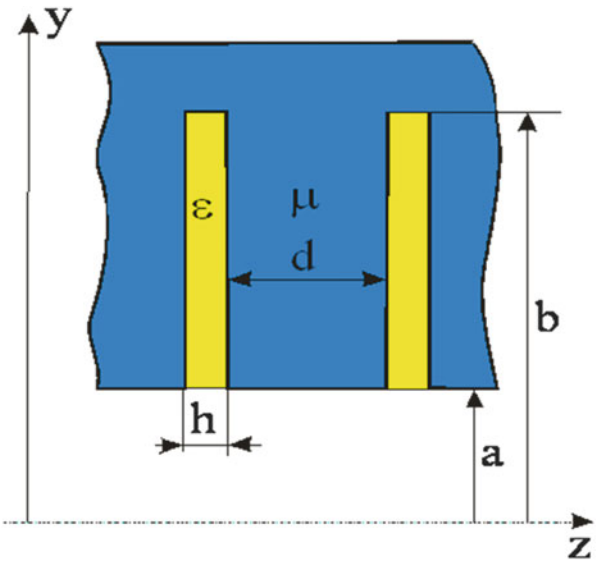


Using the boundary conditions at the metal surface, one can easily prove that the vector potential inside a thin crack satisfies the Helmholtz equation:

$$\Delta_{\perp} A^{\text{crack}} = -k^2 A^{\text{crack}}, \tag{5.7}$$

where

$$k^2 \equiv \frac{\omega^2 \varepsilon}{c^2}\left(1 + \frac{2\mu}{\kappa h}\right) \equiv \frac{\omega^2 \varepsilon}{c^2} + g^2; \quad \kappa \equiv \frac{1 - i\,\text{sgn}\omega}{\delta}$$
$$\equiv (1 - i\,\text{sgn}\omega)\frac{\sqrt{2\pi|\omega|\sigma\mu}}{c}. \tag{5.8}$$

Note that Eq. (5.7) is only justified if $gh/2 << 1$. In that case the fields inside the crack can be treated as independent from the $z$-coordinate (coordinate normal to its surface). Otherwise one need to take into account that the fields in the crack are dependent on $z$ as $\cosh(gz)$ or $\sinh(gz)$, resulting in a more complicated form for Eq. (5.7). In most practical cases, the thin crack approximation is valid. Taking into account that the crack is shorted at $y = b$, the fields can be written inside the crack as

$$\begin{aligned} A^{\text{crack}} &= A_0 \sin\left(k_y(b-y)\right); \quad k_y = \sqrt{k^2 - k_x^2}; \\ H_x^{\text{crack}} &= -k_y A_0 \cos\left(k_y(b-y)\right); \\ H_y^{\text{crack}} &= -ik_x A_0 \sin\left(k_y(b-y)\right). \end{aligned} \tag{5.9}$$

A vertical magnetic flux through the metal surface is

$$\int B_y dz\Big|_{\text{metal}} = -2ik_x\mu A_0 \sin\left(k_y(b-y)\right)/\kappa, \tag{5.10}$$

where the factor of 2 comes out due to the two sides of the lamina. Adding the flux through the crack itself, one obtains the average magnetic field, which is

$$\begin{aligned} \overline{B}_y &\equiv \frac{1}{d+h}\left(\int B_y dz\Big|_{\text{crack}} + \int B_y dz\Big|_{\text{metal}}\right) \\ &= -ik_x A_0\left(1+\frac{2\mu}{\kappa h}\right)\frac{h}{d+h}\sin\left(k_y(b-y)\right), \end{aligned} \tag{5.11}$$

yielding

$$\frac{\overline{B}_y}{H_x^{\text{crack}}}\Bigg|_{y=a+0} = \frac{ik_x}{k_y}\frac{h}{d+h}\left(1+\frac{2\mu}{\kappa h}\right)\tan\left(k_y(b-a)\right) \equiv iR_B. \tag{5.12}$$

The condition $y=a+0$ means staying vertically at $y=a+\Delta y$ so that $H,\delta << \Delta y << 1/k$. Similarly, $y=a-0$ means $y=a-\Delta y$. Since both the average magnetic field, Eq. (5.10), and the horizontal field at the crack region are preserved at crossing the magnet border $y=a$, their ratio is preserved as well:

$$\frac{\overline{B}_y}{H_x^{\text{crack}}}\Bigg|_{y=a+0} = \frac{H_y}{H_x}\Bigg|_{y=a-0}. \tag{5.13}$$

Thus, Eqs. (5.11) and (5.5) lead to the induced field amplitude

$$G = \frac{1-R_B}{1+R_B\tanh(k_x a)}. \tag{5.14}$$

At this point, only an average electric field has to be found. To do that, the Maxwell equation

$$-\frac{\partial E_z}{\partial x} + \frac{\partial E_x}{\partial z} = i\frac{\omega}{c}B_y \tag{5.15}$$

can be averaged over a period, yielding

$$\overline{E}_z\Big|_{y=a+0} = -\frac{\omega}{ck_x}\overline{B}_y\Big|_{y=a+0}. \tag{5.16}$$

Average electric fields above and below the boundary (with a thickness of $\Delta y$) are related as

$$\overline{E}_z\big|_{y=a+0} - \overline{E}_z\big|_{y=a-0} = i\frac{\omega\mu}{\kappa c} H_x|_{y=a-0}. \tag{5.17}$$

Using Eq. (5.14), the horizontal field is found:

$$H_x|_{y=a-0} = \frac{\partial A}{\partial y} = -\frac{Z_0 I_0}{2\cosh(k_x a)} \frac{1}{1 + R_B \tanh(k_x a)}. \tag{5.18}$$

Finally Eqs. (5.18), (5.16), and (5.11) yield the following result:

$$Z_{\|} = -\frac{1}{I_0}\int_0^\infty \overline{E}_z\big|_{y=0}\frac{dk_x}{\pi} = -i\frac{\omega}{c}\frac{Z_0}{2\pi}\int_0^\infty \frac{dk_x}{k_x}\frac{R_B + \mu k_x/\kappa}{\cosh^2(k_x a)(1 + R_B\tanh(k_x a))}, \tag{5.19}$$

for the longitudinal impedance per unit length. Here we used that

$$\overline{E}_z\big|_{y=0} = \frac{\overline{E}_z\big|_{y=a-0}}{\cosh(k_x a)}. \tag{5.20}$$

### 5.2.2 *Flat Chamber: Transverse Impedances*

For the horizontal beam oscillations, the vector potential is an even function of the vertical coordinate and odd one of the horizontal; according to [17]:

$$A = -i\frac{D_0 Z_0}{2}\left[\exp(-k_x y) - G\frac{\cosh(k_x y)}{\cosh(k_x a)}\exp(-k_x a)\right];\ \ k_x > 0,\ \ 0 < y < a, \tag{5.21}$$

with $D_0$ as the amplitude of the beam dipole moment oscillations. Note that this field differs from the longitudinal case, Eq. (5.4), only by the amplitude; thus, all the field ratios remain the same. In particular, Eq. (5.14) is valid for this case as well. Using Eqs. (10, 11) of [17], the horizontal impedance follows:

$$\begin{aligned} Z_x &= Z_x^\sigma + Z_x^\infty \\ &= -i\frac{Z_0\beta}{2\pi}\int_0^\infty \frac{(R_B + \mu k_x/\kappa)k_x dk_x}{\cosh^2(k_x a)(1 + R_B\tanh(k_x a))} - i\frac{Z_0}{2\pi a^2\beta\gamma^2}\frac{\pi^2}{24}. \end{aligned} \tag{5.22}$$

The vertical impedance can be found from the horizontal by a substitution $\cosh(k_x a) \leftrightarrow \sinh(k_x a)$ in the finite conductance term $Z_x^\sigma$ and taking twice higher infinite conductivity term [17]

$$Z_y = Z_y^\sigma + Z_y^\infty$$
$$= -i\frac{Z_0\beta}{2\pi}\int_0^\infty \frac{(R_B + \mu k_x/\kappa)k_x dk_x}{\sinh^2(k_x a)(1 + R_B\coth(k_x a))} - i\frac{Z_0}{2\pi a^2\beta\gamma^2}\frac{\pi^2}{12}. \tag{5.23}$$

Note that the second terms in the integrand numerator in Eqs. (5.19), (5.22), and (5.23) ($\mu k_x/\kappa$) yield the conventional resistive wall impedances when the crack width approaches zero.

### 5.2.3 Round Chamber: Longitudinal Impedance

For a round vacuum chamber of radius $a$ and arbitrary walls, the axially symmetric fields in the free space are related so that (Eq. (2.3) in [19])

$$H_\varphi = \frac{2I_0}{rc} - i\frac{\omega r}{2c}E_z, \;\; r < a. \tag{5.24}$$

From here, the longitudinal impedance $Z_{||}$ can be related to the so-called surface impedance $R$:

$$Z_{||} = -\frac{E_z}{I_0} = \frac{Z_0}{2\pi a}\frac{R}{1 - i\omega aR/(2c)}; \quad R \equiv -E_z/H_\varphi\big|_{r=a-0}. \tag{5.25}$$

The Maxwell equation $\nabla \times \mathbf{E} = i\omega\mathbf{B}/c$, applied to the azimuthal direction, relates inner and outer average longitudinal electric fields (compare with Eq. (5.17)):

$$\overline{E}_z\big|_{r=a+0} - \overline{E}_z\big|_{r=a-0} = -i\omega\mu H_\varphi/(\kappa c). \tag{5.26}$$

This can also be written as

$$R = R_+ - i\frac{\omega\mu}{\kappa c}; \quad R_+ \equiv -\frac{\overline{E}_z\big|_{r=a+0}}{H_\varphi} \tag{5.27}$$

Inside the crack, the longitudinal electric field satisfies the Helmholtz equation (compare with Eq. (5.6)):

$$\begin{aligned} \Delta_\perp E_z^{\text{crack}} &= -k^2 E_z^{\text{crack}}; \\ H_\varphi^{\text{crack}} &= i\frac{\omega\varepsilon}{k}\frac{\partial E_z^{\text{crack}}}{\partial(kr)}. \end{aligned} \tag{5.28}$$

From here, the field components are expressed in terms of the Hankel functions:

$$E_z^{\text{crack}} = E_0\left[H_0^{(1)}(kr)H_0^{(2)}(kb) - H_0^{(2)}(kr)H_0^{(1)}(kb)\right];\\ H_\varphi^{\text{crack}} = -i\frac{\omega\varepsilon}{ck}E_0\left[H_1^{(1)}(kr)H_0^{(2)}(kb) - H_1^{(2)}(kr)H_0^{(1)}(kb)\right]. \tag{5.29}$$

A factor $\cosh(gz)$ is omitted according to the assumption $gh/2 << 1$. Since there is no longitudinal electric field in the metal, only the crack electric field contributes to its average:

$$\overline{E}_z\Big|_{r=a+0} = E_z^{\text{crack}}\frac{h}{d+h}. \tag{5.30}$$

Together with Eq. (5.29), this yields

$$R_+ \equiv -\frac{\overline{E}_z}{H_\varphi^{\text{crack}}}\Bigg|_{r=a+0}\\ = -i\frac{ckh}{\omega\varepsilon(d+h)}\frac{H_0^{(1)}(ka)H_0^{(2)}(kb) - H_0^{(2)}(ka)H_0^{(1)}(kb)}{H_1^{(1)}(ka)H_0^{(2)}(kb) - H_1^{(2)}(ka)H_0^{(1)}(kb)}. \tag{5.31}$$

With Eq. (5.27), the impedance in Eq. (5.25) follows:

$$Z_{||} = \frac{Z_0}{2\pi a}\frac{R_+ - i\omega\mu/(\kappa c)}{1 - i\frac{\omega a R_+}{2c} - \frac{\omega^2 a\mu}{2\kappa c^2}}, \tag{5.32}$$

where the second term in the numerator is responsible for the conventional resistive wall impedance when the cracks disappear.

### 5.2.4 Round Chamber: Transverse Impedances

For the transverse dipole oscillations, the vector potential in the free space can be written as

$$A = \frac{2D_0}{ca}\left(\frac{a}{r} - G\frac{r}{a}\right)\cos\varphi \equiv A_0\left(\frac{a}{r} - G\frac{r}{a}\right)\cos\varphi, \tag{5.33}$$

where $D_0$ is the amplitude of the dipole moment oscillations. In terms of the induced field amplitude $G$, the transverse impedance is expressed as [18]

$$Z_\perp = Z_\perp^\sigma + Z_\perp^\infty = -i\frac{Z_0\beta(1-G)}{2\pi a^2} - i\frac{Z_0}{2\pi a^2\beta\gamma^2}. \tag{5.34}$$

At the inner border, $r=a-0$, the longitudinal electric and azimuthal magnetic fields follow as

$$\begin{aligned} E_z &= i\omega A/c = i\omega A_0(1-G)\cos\varphi/c; \\ H_\varphi &= -\partial A/\partial r = A_0(1+G)\cos\varphi/a. \end{aligned} \tag{5.35}$$

This relates the surface impedance $R = -E_z/H_\varphi|_{r=a-0}$ and the induced field amplitude $G$

$$R = -i\frac{\omega a}{c}\frac{1-G}{1+G} \Leftrightarrow 1-G = \frac{2R}{R - i\omega a/c}. \tag{5.36}$$

Note that although the fields $E_z, H_\varphi$, etc. and their ratios $R, R_+$ are denoted by the same symbols for the longitudinal and the transverse cases, they are not the same and should not be confused. Inside the crack, the field components $E_z^{\text{crack}}, H_\varphi^{\text{crack}}$ satisfy Eq. (5.28), leading for the dipole mode to

$$\begin{aligned} E_z^{\text{crack}} &= E_0\left[H_1^{(1)}(kr)H_1^{(2)}(kb) - H_1^{(2)}(kr)H_1^{(1)}(kb)\right]\cos\varphi; \\ H_\varphi^{\text{crack}} &= i\frac{\omega\varepsilon}{ck}E_0\left[H_1^{(1)'}(kr)H_1^{(2)}(kb) - H_1^{(2)'}(kr)H_1^{(1)}(kb)\right]\cos\varphi. \end{aligned} \tag{5.37}$$

For the calculations, it is useful to remember the derivatives of the Hankel functions are expressed as

$$H_1'(x) = [H_0(x) - H_2(x)]/2. \tag{5.38}$$

Equation (5.37) yields the field ratio

$$\begin{aligned} R_+ &\equiv -\frac{\overline{E}_z}{H_\varphi^{\text{crack}}}\bigg|_{r=a+0} \\ &= i\frac{ckh}{\omega\varepsilon(d+h)}\frac{H_1^{(1)}(ka)H_1^{(2)}(kb) - H_1^{(2)}(ka)H_1^{(1)}(kb)}{H_1^{(1)'}(ka)H_1^{(2)}(kb) - H_1^{(2)'}(ka)H_1^{(1)}(kb)}. \end{aligned} \tag{5.39}$$

With Eqs. (5.27) and (5.36), this formula yields the transverse impedance Eq. (5.34)

$$\begin{aligned} Z_\perp &= Z_\perp^\sigma + Z_\perp^\infty = -i\frac{Z_0\beta}{\pi a^2}\frac{R}{R - i\omega a/c} - i\frac{Z_0}{2\pi a^2\beta\gamma^2}; \\ R &= R_+ - i\frac{\omega\mu}{\kappa c} = i\frac{ckh}{\omega\varepsilon(d+h)}\frac{H_1^{(1)}(ka)H_1^{(2)}(kb) - H_1^{(2)}(ka)H_1^{(1)}(kb)}{H_1^{(1)'}(ka)H_1^{(2)}(kb) - H_1^{(2)'}(ka)H_1^{(1)}(kb)} - i\frac{\omega\mu}{\kappa c}. \end{aligned} \tag{5.40}$$

### 5.2.5 Impedances of the Booster Laminated Chamber

It would be good to discuss the impedances on a base of real parameters of the Booster magnets. However, some of the important parameters are actually unknown. While the inner and outer aperture $a$ and $b$ as well as the lamina thickness $d$ are perfectly known, we have a poor knowledge of the magnetic permeability $\mu$ at the interesting frequency range of hundreds MHz. Moreover, the guiding magnetic field makes that value not just a function of frequency but a tensor function. Another uncertainty relates to the crack width $h$. Comparison of the average lamina thickness with the entire length of the magnet gives only a magnet-average value for $h$. There is no reason to assume that these values have a narrow distribution near their average. Ideally, the calculated impedances have to be averaged over this distribution—but it cannot be done even approximately without knowing the rms spread of the crack widths. One more uncertainty relates to thickness of the iron oxide at the lamina surfaces, which may change the crack properties. All these uncertainties can be reduced with a set of dedicated measurements, and some of them are reported in [21]. Longitudinal impedances for the Booster focusing magnet (see its parameters in Table 5.2) calculated using Eq. (5.19), (5.32) are shown in Fig. 5.7 and are in a good agreement with the measurements of [21].

Several features of Fig. 5.7 deserve to be noted:

1. The low limit of the frequency range is determined by the skin depth: at 10 kHz $\delta \approx d/2$.
2. At low frequencies, $f \ll 50$ MHz, a simplistic electrotechnical approximation $Z_{||} = \frac{\kappa}{\pi d\sigma}\ln(b/a) = Z_{||}^{\mathrm{conv}}\frac{2a}{d}\ln(b/a) \propto \omega^{1/2}$ for the round geometry coincides with the actual solution. In the case of flat aperture, the low-frequency impedance scaling is different, $Z_{||} \propto \omega^{3/4}$.
3. Note that impedance of the conventional solid vacuum chamber $Z_{||}^{\mathrm{conv}} = \frac{\kappa}{2\pi a\sigma}$ exceeds the careless limit $|Z_{||}/n| \leq Z_0/2$ [19] by a factor of $(\mu\delta/a)\ln(b/a)$. For $\mu >> 1$ this can be a big number. The reason is that the field energy located inside the magnetic chamber grows unlimitedly with the magnetic permeability: $\frac{\mu H^2}{8\pi}2\pi a\delta \propto \sqrt{\mu}$.
4. A limit for the low-frequency approximation is determined by the field decay along the crack depth, $\mathrm{Im}k \propto \omega^{3/4}$ (see Eq. (5.7)). At sufficiently high frequency, when $\mathrm{Im}\,kb >> 1$, this radial field decay limits the length of the shielding current along the crack surface before it reaches the outer shortcut radius $b$. At $f > 1$ GHz, $\mathrm{Im}ka \geq 1$, so the path length of the shielding current gets proportional to the field decay length $\mathrm{Im}k$, leading to $Z_{||} \approx Z_{||}^{\mathrm{conv}}\frac{2}{d\mathrm{Im}k} \propto \omega^{-1/4}$.
5. For usual, not-laminated vacuum chambers, the longitudinal impedance of the flat chamber is known to be equal to one of the round chamber [22, 23]. In other words, the longitudinal Yokoya factor of the solid flat chamber or the ratio of flat-to-round impedances is 1. As it is seen from Fig. 5.7, the Yokoya factor of the flat laminated chamber is close to 1 at $f \geq 10$ MHz, while at lower frequencies, it may be significantly smaller.

**Table 5.2** Accepted parameters of the Booster F-magnet

| | | |
|---|---|---|
| $a$ | Magnet half gap | 2.08 cm |
| $b$ | Outer shortcut | 16.5 cm |
| $d$ | Lamina thickness | 0.064 cm |
| $h$ | Crack width | 0.002 cm |
| $\sigma$ | Conductivity | $4.5 \cdot 10^{16}$ 1/s |
| $\varepsilon$ | Dielectric permittivity | 4.75 |
| $\mu$ | Magnetic permeability | 50 |

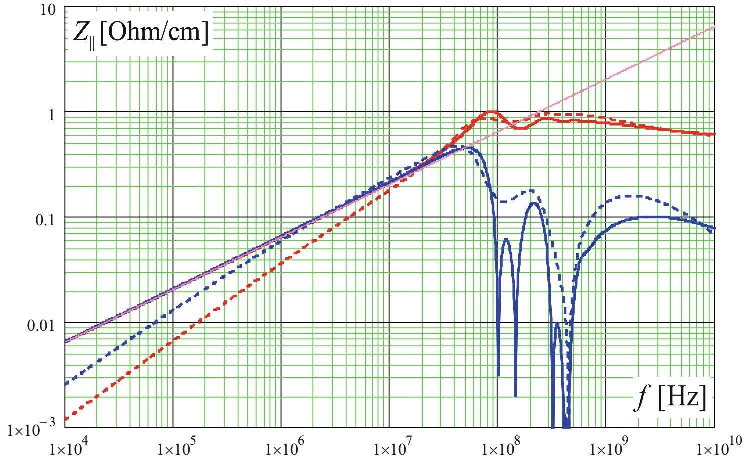


**Fig. 5.7** Longitudinal impedances for the round (*solid lines*) and flat (*dash lines*) geometries. *Red lines* are for the real parts, and *blue* for the absolute value of the imaginary parts. The *magenta line* shows the low-frequency approximation $\mathrm{Re}Z_{\|}^{\mathrm{LF}} = \frac{1}{\pi d \sigma \delta} \ln(b/a) = \mathrm{Re}Z_{\|}^{\mathrm{conv}} \frac{2a}{d} \ln(b/a)$ with $Z_{\|}^{\mathrm{conv}} = \frac{\kappa}{2\pi a \sigma}$ as longitudinal impedance of the conventional solid round vacuum chamber of the same metal

The transverse impedances are presented in Fig. 5.8. There are several reasons for the complicated behavior of the transverse impedances. First, the depth of field penetration inside the crack changes at $ka > 1$. Above that frequency (~1 GHz), the shielding current path length is determined by the decay along the crack, while below that it is determined by the aperture $a$.

The second reason is change of the field structure at $|Rc/(\omega a)| \sim 1$, equivalent to $\mu\delta/d \sim 1$ or $f \sim 10$ MHz. At low frequencies, when $\mu\delta/d > 1$, the fields inside the free space, $r < a$, are of the magnetic type: the magnetic field is almost orthogonal to the magnet surface, $|H_\phi/H_r|_{r=a-0} \sim 1$. In the opposite case, for $\mu\delta/d < 1$, the fields are close to those of the conducting wire: $|H_\phi/H_r|_{r=a-0} >> 1$. Interplay of these and some geometrical factors leads to variety of possibilities for impedance behavior at low frequencies seen in Fig. 5.8. Note, contrary to the longitudinal impedance, the transverse one never exceeds its careless limit $Z_0\beta/(\pi a^2)$. That is why a popular Panofsky-Wenzel estimation of the transverse impedance from the longitudinal is

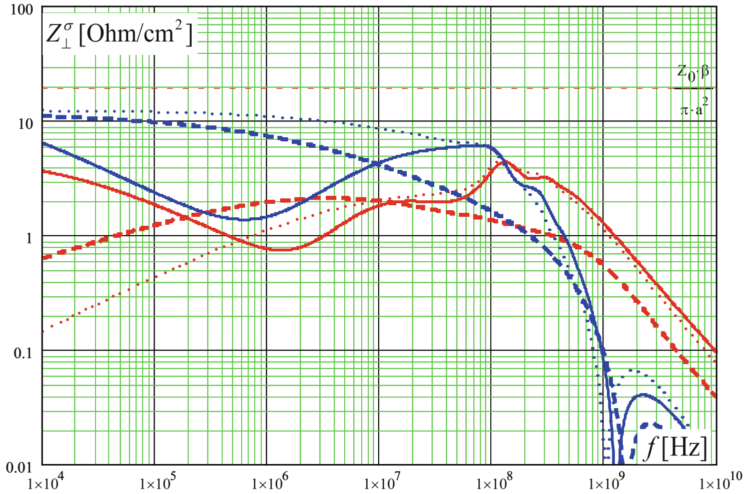


**Fig. 5.8** Transverse impedances ($\gamma \to \infty$) for the round (*solid lines*) and flat geometry (*dash lines* for the horizontal and *dot lines* for the vertical). *Red lines* are for the real parts, and *blue* for the absolute value of the imaginary parts

inapplicable here: its use at low frequencies may result in order(s) of magnitude overestimation for the transverse impedance.

## 5.3 Transverse Instability of Antiprotons in the Recycler

In the course of typical store (of about 16 hours) up to $5 \times 10^{12}$ antiprotons are accumulated and cooled in Recycler. The reduction of the cooled antiproton beam emittances is limited by a transverse instability [24]. Since the antiprotons are, for the most part, accumulated within long bunches, where synchrotron oscillations are slow enough to be neglected, a coasting beam model [25] appears to be a reasonable first approximation to the stability problem. However, it was realized—both theoretically and experimentally—that the stability thresholds [26] and the spatial behavior of the unstable modes [19, 27] differ from the simplified expectations of the coasting beam model.

### *5.3.1 Stability of Coasting Beam*

A beam stability threshold is determined by an equality of the Landau damping rate $\Lambda$ and the impedance-driven growth rate: $\Lambda = \Omega_0 \mathrm{Im} \Delta Q_c$. For the coasting beam with space charge-dominated impedance, $|\Delta Q_c| << |\Delta Q_{sc}|$, the growth rate can be easily calculated, since the lattice tune spread can be neglected for that purpose (see, e.g., [19]; Eq. (5.88)). Following [25], the damping rate can be expressed as

$$\begin{aligned} \Lambda &= -\pi\Omega_0 \langle \Delta Q_{\mathrm{sc}} \rangle \int \Delta Q_{\mathrm{sc}} f_x J_x \;\; \delta(\Delta Q_l + \Delta Q_{\mathrm{sc}}) d\Gamma \;\;, \\ \langle \Delta Q_{\mathrm{sc}} \rangle &\equiv -\left( \int \frac{f_x J_x \;\; d\Gamma}{\Delta Q_{\mathrm{sc}}} \right)^{-1} \;\;, \end{aligned} \tag{5.41}$$

where $\Delta Q_{\mathrm{sc}} = \Delta Q_{\mathrm{sc}}(J_x, J_y)$ is the space charge tune shift as a function of the two transverse actions, $f_x = \partial f / \partial J_x$ is a partial derivative of the normalized phase-space density $\int f dJ_x dJ_y dp \equiv \int f d\Gamma = 1$ with $p$ as the relative momentum offset, and $\Delta Q_l = \Delta Q_l(J_x, J_y, p)$ is the lattice tune shift due to nonlinearity and chromaticity $\xi$. For the Gaussian distribution and a round beam, the chromaticity-related threshold is well approximated by [25]:

$$\frac{|\Delta Q_{\mathrm{sc}}(0)|}{\sigma_{\nu p}} = 1.7 \ln\left( \frac{|\Delta Q_{\mathrm{sc}}(0)|}{\mathrm{Im}\Delta Q_c} \right), \tag{5.42}$$

where

$$\sigma_{\nu p} = |\xi - n\eta - Q\eta| \sigma_p \equiv \xi_n \sigma_p$$

is the effective chromatic rms tune spread for mode $n$ with effective chromaticity $\xi_n$, $\Delta Q_{\mathrm{sc}}(0)$ is the space charge tune shift at the center of the beam, and $\sigma_p$ is the rms momentum spread.

Note that the Landau damping rate is determined by the integral over a surface of the resonant particles, whose individual tune shifts $\Delta Q_{\mathrm{sc}} + \Delta Q_l$ are equal to the coherent tune shift $\mathrm{Re}\Delta Q_c$. For the space charge-dominated impedances, $|\Delta Q_c| \ll |\Delta Q_{\mathrm{sc}}|$, the coherent tune shift can be neglected in the argument of the delta-function in Eq. (5.41). If the lattice tune spread is determined by the chromaticity only, the resonant surface is represented as

$$\xi_n \frac{\Delta p}{p} + \Delta Q_{\mathrm{sc}} = \mathrm{Re}\Delta Q_c \approx 0.$$

Therefore, the maximum momentum offset of the resonant particles $\Delta p_{\mathrm{res\_max}}$ is equal to

$$\Delta p_{\mathrm{res\_max}} = \left| \frac{\Delta Q_{\mathrm{sc}}(0)}{\xi_n} p \right|. \tag{5.43}$$

For operational purposes, the instability threshold was expressed and measured in terms of the effective phase-space density:

$$D_{95\%} = \frac{N[E10]}{\varepsilon_{(\perp)n,95\%}[\mathrm{mm} \times \mathrm{mrad}] \cdot \varepsilon_{(s)n,95\%}[\mathrm{eV} \times \mathrm{s}]}, \tag{5.44}$$

where $N$ is the number of antiprotons, $\varepsilon_{(\perp)n,95\%}$ is the normalized 95 % emittance, and $\varepsilon_{(s)n,95\%}$ is the longitudinal 95 % emittance for the barrier-bucket RF; the units are shown in the square brackets—see also Eq. (5.1). For the Gaussian distribution, the 95 % emittances are related to the rms emittances as $\varepsilon_{(\perp)n,95\%} = 6\varepsilon_{(\perp)n}$, $\varepsilon_{(s)n,95\%} = 4\varepsilon_{(s)n}$. In terms of the density, Eq. (5.44), the instability threshold, Eq. (5.43), can be expressed as

$$D_{95\%} = 60F \frac{\gamma_0^2 \xi_n}{T_0[\mathrm{s}] E_0[\mathrm{eV}]} \quad , \quad F \equiv \ln\left(\frac{|\Delta Q_{\mathrm{sc}}(0)|}{\mathrm{Im}\Delta Q_c}\right); \tag{5.45}$$

units for the revolution time $T_0$ and the beam energy $E_0 = \gamma_0 m_p c^2$ are shown in the brackets. Since the effective chromaticity and the coherent tune shift depend on the mode frequency, or the harmonic number $n$, so does the instability threshold. If there are no external feedbacks, the threshold is determined by the mode which gives the lowest density value, Eq. (5.45). For the resistive wall impedance, it is the lowest betatron sideband of the slow waves. When a broadband damper is applied, then for the resistive wall impedance, the beam is most unstable for a wave at the frequency edge of the damper, ~70 MHz for the Recycler. For identical chromaticities and damper bandwidths, the horizontal instability cannot be seen, since the vertical resistive wall impedance is a factor of 2 higher than the horizontal, making the vertical threshold slightly lower due to the logarithmic factor $F$. However, this slight logarithmic difference can be outweighed by a small difference in the effective chromaticities $\xi_{nx}$ and $\xi_{ny}$ of Eq. (5.42) if the absolute value of the vertical chromaticity sufficiently exceeds that of the horizontal. When the normal chromaticities $\xi_{x,y}$ are small and the effective chromaticities are dominated by the longitudinal factor $n\eta$, polarization of the instability depends on an interplay of these two weak factors and may spontaneously change due to a small uncontrolled variation in the chromaticities.

The threshold expressions in Eqs. (5.42) and (5.45) should be used with some caution. The coherent motion is stabilized by resonant particles, whose individual lattice tune shift compensates their individual space charge tune shift, Eq. (5.41). For the space charge-dominated impedance, these particles are in the far tails—longitudinal and transverse—of the beam distribution. When electron cooling is applied, there is no reason to assume the distribution to be Gaussian, so, strictly speaking, Eqs. (5.42), (5.45) are not applicable. These far tails of the distribution are not measurable, so the general formula in Eq. (5.41) cannot be used either. In this situation, the threshold value of the phase density is found experimentally. It may deviate from the value for a Gaussian distribution by up to a factor of 2 in both directions. Additional reasons for the discrepancy between calculations and measurements are discussed below.

### 5.3.2 Bunching Effects

Even if the synchrotron tune is much smaller than the coherent tune shift, there are at least three different ways for which the beam bunching may influence the coherent oscillations.

First, for a bunch with a negligible synchrotron tune, the tail-to-head interaction takes place due to a long-range wake field (left from previous revolutions). This leads to a dependence of the coherent tune shift $\Delta Q_c$ on the bunching factor $B = T_0/\tau_0 \geq 1$ [27, 28]. The Recycler's wake field is believed to be dominated by the resistive wall contribution; thus, the coherent tune shift slowly grows when the bunch length decreases; for a single bunch in the ring $\Delta Q_c \propto B^{1/3}$ [28], close to a two-particle model where $\Delta Q_c \propto B^{1/4}$ [27]. Note that this leads only to a slow logarithmic growth of the stability threshold in Eq. (5.45), mostly due to $\Delta Q_{\rm sc} \propto B$.

For a barrier bucket with "infinite walls", the above consideration is the only correction to be applied to the coasting beam model. However, the RF voltage $V_{\rm RF}$ and the barrier width $\tau_{\rm b}$ are limited, so a second effect from bunching takes place: particles with sufficient momentum offset $|p| \geq p_{\rm dc} = \sqrt{2V_{\rm RF}\tau_{\rm b}/(|\eta|E_0T_0)}$ are leaving the potential well and spend most of their time outside of the bucket (the so-called DC beam). If the barriers are lower than $\Delta p_{\rm res\_max}$ in Eq. (5.43), some of the particles responsible for Landau damping do not contribute anymore, and the beam is less stable than it would be with a deeper potential well. Contrary to the first effect of the bunching factor, this one leads to a decrease of the instability threshold the more compressed the bunch is with the same barriers. Indeed, by compressing the bunch, the momentum offset of the AC particles grows, and some resonant particles spill outside the potential well and become DC.

A third factor, which would alter the coasting beam model, is the possibility for the potential well profile to depart from the one resulting from a barrier RF configuration. Before extraction, the beam is kept inside cosine-like potential wells; hence the barrier-bucket theory does not apply. Similar to head-tail modes with strong space charge, where smooth walls of the potential well are better for Landau damping [29], the beam stability threshold for this case can be expected to increase as well.

Finally, it should be mentioned that the presence of multiple bunches around the Recycler also affects the way an instability develops. Indeed, other bunches play the role of "relay stations" for the tail-head signal, thus increasing the coherent growth rate $\Omega_0 \mathrm{Im}\Delta Q_c$ and in turn logarithmically decreasing the instability threshold.

### 5.3.3 Longitudinal Bunch Tomography

The above arguments indicate that the density threshold in Eq. (5.45) should depend on the shape of RF well. To study this dependence, a longitudinal tomography diagnostic was developed and applied to the Recycler. The idea for that tomography is based on the fact that for a given RF shape, a bunch longitudinal profile provides information about the phase-space density [30]. Thus, measured RF and bunch profiles allow calculating the distribution function of the bunch. This is attained by solving the following set of equations:

$$
\begin{aligned}
&H(\varepsilon,\tau) = \frac{\varepsilon^2}{2\mu} + W(\tau);\\
&W(\tau) = -\frac{1}{T_0}\int_0^{\tau} V_{\mathrm{RF}}(t)dt;\\
&\lambda(W) = \int_{-\infty}^{\infty} f(H(\varepsilon,\tau))d\varepsilon = \sqrt{2\mu}\int_W^{H_{\max}} \frac{f(H)}{\sqrt{H-W}}\,dH;\\
&I(H) = \frac{1}{2\pi}\oint \varepsilon(H,\tau)\,d\tau.
\end{aligned}
\tag{5.46}
$$

Here $H(\varepsilon,\tau)$ is the Hamiltonian as a function of its canonical variables $\varepsilon$ (the energy offset) and $\tau$ (the timing offset), $V_{\mathrm{RF}}(t)$ is the RF voltage at time $t$, $W(\tau)$ is the potential energy at position $\tau$, $p_0 = \beta_0 E_0/c$ is the beam momentum, $\mu = p_0 c/|\eta|$ is the effective mass, $\lambda(W)$ is the beam linear density as a function of the potential $W$ (taken from measurements), $f(H)$ is the phase-space density as a function of the Hamiltonian to be found, $I(H)$ is the action variable, $f_I(I) = f(H(I))$, and $H_{\max}$, $I_{\max}$ are the maximal Hamiltonian and action inside the bucket; DC particles are neglected. A solution of Eq. (5.46) can be presented in terms of the integrated distribution or the fraction of particles inside a given action $G(I) = \int_0^I f_I\left(I'\right)dI' / \int_0^{I_{\max}} f_I\left(I'\right)dI'$. Then, its inverse function $2\pi I(G)$ gives the longitudinal emittance, or the phase space, as a function of the percentage of particles contained inside that phase space. Tomography analyses for the Recycler are described in some more details in [31].

### 5.3.4 Observations

Several cases of beam instabilities were observed in the Recycler without external damping. In these cases, the measured instability threshold was in reasonable agreement with Eq. (5.45) (see [32]) and corresponded to $D_{95\%} = 0.5$–$0.8$. The scatter in the threshold values was due to the limited accuracy of the emittance measurements, the uncertainty of the chromaticity value, and variations in the tail distribution. The other features of the instability were also in line with theoretical predictions. The beam became unstable at the lower betatron sideband primarily in the vertical direction. The coherent oscillations grew for several dozens of turns until a partial beam loss occurred.

To counteract the instability, two transverse dampers (vertical and horizontal) were installed, initially with the bandwidth of 35 MHz [32]. Several studies performed with the antiproton beam in the standard configuration (a "rectangular" barrier bucket with standard barrier height of ~17 MeV/c) clearly showed, as expected, a significant increase of the instability threshold as a result of the dampers installation but again with a sizeable scatter in the threshold $D_{95\%}$. In fact, in one occasion, without turning the dampers off, the instability could not be provoked at all up to $D_{95\%} = 3.1$. Note that turning the dampers off resulted in a fast (<0.1 s) beam loss. However, in two other studies, the beam went unstable at $D_{95\%} = 3.0$ and 2.6.

An important operational limitation was found to be the saturation of the dampers' pickup preamplifiers. It was observed during beam preparation for extraction, when the linear beam density increases by more than a factor of 2. Saturation was effectively turning off the dampers, and the developing instability and accompanying beam loss yielded "clipping" all bunches down to the same peak density.

With advances in the strength of electron cooling and increasing requirements to the beam brightness in the Recycler, the dampers bandwidth became insufficient and started to affect the regular operation of the collider. Therefore, the dampers were upgraded in December 2007. The upgraded version, which has been in use until the end of Run II, had an effective bandwidth of ~70 MHz, and the preamplifiers' saturation limit was increased [33]. For this bandwidth ($n \approx 780$) and typical beam parameters ($Q'' = -4$, $\varepsilon_{(a)(\perp)n,95\%} = 2\,\pi$ mm mrad, $B = 0.5$), Eq. (5.45) predicts the threshold phase density of $D_{95\%} = 4.3$. In measurements, the instability threshold was increased to $D_{95\%} = 4.3$–6.9. These numbers show the scatter of several studies carried out with the antiproton beam contained in a rectangular bucket with the standard barrier height (17 MeV/c). In the regular operation, the phase density was kept below 2.7 to guaranty beam stability. However, on a few occasions, the instability still did develop during extraction. The extraction process includes complicated manipulations in the longitudinal phase space, described in detail in Chap. 4. Nevertheless, to illustrate better the extraction process, the three main RF configurations and associated beam longitudinal profiles are shown again in Fig. 5.9. First, the bunch is divided into nine nearly identical pieces by narrow rectangular barriers (called for historical reasons "mined bunches"). Then antiprotons are moved, one mined bunch at a time, into the extraction region. Once there, a mined bunch is adiabatically transformed into four 2.5 MHz smaller bunches, which are then extracted into the matching main injector (MI) RF waveform.

With the dampers in the final configuration (2008–2011), the instability was observed six times in the course of extraction. All of them were similar and had the following main characteristics:

1. The beam loss occurs during the second half of the extraction process.
2. Only one mined bunch at a time goes unstable.
3. Typically, after the first instability, all remaining bunches become unstable as well at later stages. In a couple of exceptions, the very last bunch (#9) remained stable. In those cases, the bunch #9's intensity was ~20 % lower than other bunch intensities because of imperfections of the RF voltage.

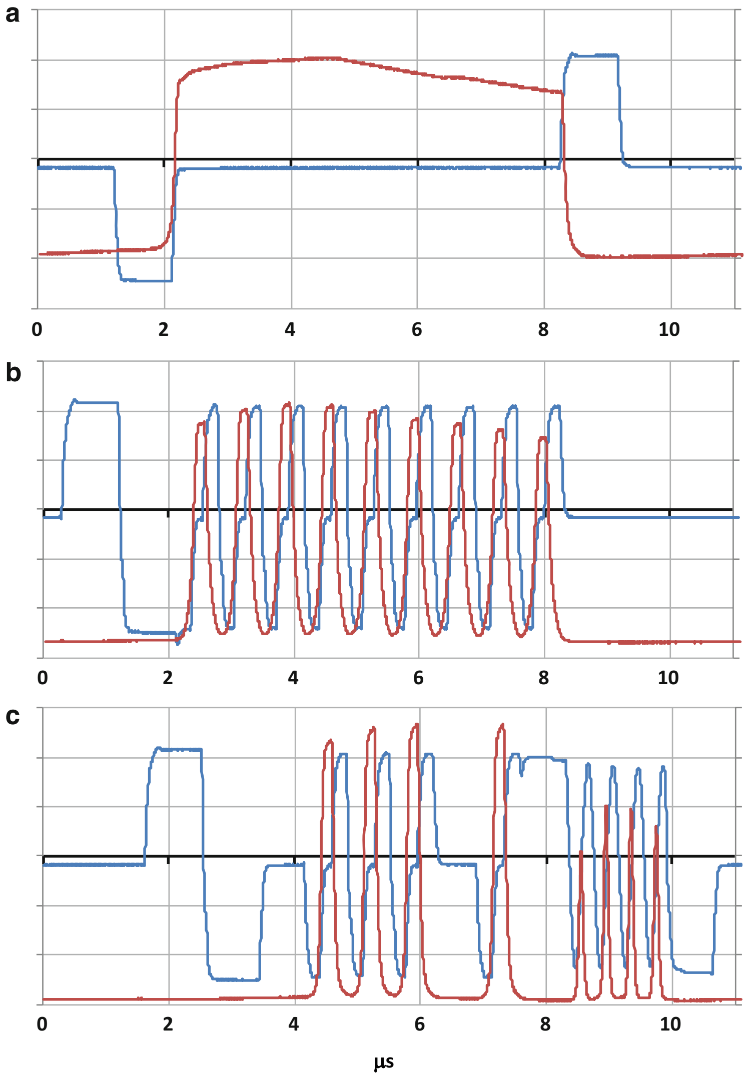


**Fig. 5.9** RF voltage (*blue line*) and beam longitudinal profile (measured by the resistive wall monitor, RWM, *red line*) waveforms recorded during an extraction to the Tevatron. (**a**) “Cold” bucket, (**b**) nine mined buckets, and (**c**) mined buckets + 2.5 MHz structure on the bunch which is in the extraction region after having already extracted four “mined” bunches. *Vertical scales* are arbitrary. Note that in case (**a**), the beam longitudinal profile deviates from the rectangular distribution expected for a beam stored within two RF barriers because of the RF imperfection

4. Each beam loss lasts 5–15 s.
5. Traces are recorded with the damper pickups (Fig. 5.10) during 32 ms after detecting the instability. They show that the instability happens at the frequency right outside of the damper bandwidth, ~70 MHz. Only a 100–200 ns portion of

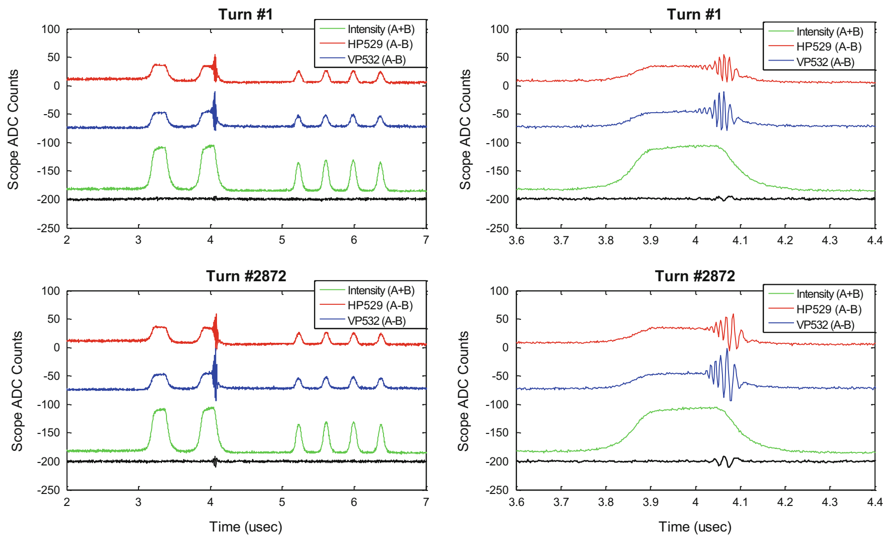


**Fig. 5.10** Oscilloscope traces of the transverse damper pickup signals during instability: on the *left* (**a**, **b**), one full revolution for turns #1 and #2872; on the *right* (**c**, **d**), focus on the bunch that went unstable (Bunch #8). The *vertical scale* is arbitrary. The *green trace* is the sum signal and is proportional to the linear density distribution. The *red* and *blue traces* are the difference (not normalized) signals for two damper pickups (*red*: horizontal; *blue* vertical) and reflect the beam transverse position. The *black trace* is the damper vertical kick amplitude. *Top* plots (**a**) and (**c**) are at the early stage of the instability development; *bottom* plots (**b**) and (**d**) are at the end of the recording period of 32 ms

the bunch oscillates. It is located either at the bunch tail or around the maximum of its linear density. The length of the oscillating portion does not change within the recorded 32 ms. During that time, the oscillations exhibit only a modest growth, less than two times their amplitude. Also, no significant changes in the bunch intensity are observed.

Note that the traces in Fig. 5.10 show that both the horizontal and vertical directions went unstable although the largest emittance growth was seen in the vertical direction. This particular case points to the possibility that the instability threshold in the horizontal direction can become very close to (even exceed) the vertical's due to uncontrolled variations of their respective chromaticities. Figure 5.10 also shows almost no response from the dampers kickers because of the frequency response limit discussed above.

The beam phase density was similar at different stages of the extraction process; however, the instabilities occurred only for bunches in one of the RF configurations, the so-called "the mined" bucket. This peculiarity was explained by the combination of the high linear density and low barrier height (8.5 MeV/c vs. standard 17 MeV/c) in this configuration. It leads to an effective exclusion from Landau damping of antiprotons with high longitudinal, low transverse actions. This hypothesis was tested in a dedicated study, where the beam stability was compared in different RF configurations. It was found that lowering the height of the barrier potential by a factor of 2, mimicking what happens for the mined bunches, decreased the threshold phase density $D_{95\%}$ from 6.9 to 4.5.

As in all previous instances, the threshold value of $D_{95\%}$ was calculated using the average 95 %, normalized transverse emittance, $(\varepsilon_{(x)n,95\%} + \varepsilon_{(y)n,95\%})/2$, and the longitudinal emittance. Both measurements are based on signals from the 1.7 GHz Schottky pickups, with the longitudinal emittance calculation done assuming a rectangular bucket and a Gaussian momentum distribution.

The Schottky power is proportional to the square of the rms beam size times the number of particles, i.e., $P_{\text{Schottky}} \propto \sigma^2 \times N$. To calibrate the emittances measured with the Schottky detector, a method that employs beam scrapers with a relatively low intensity beam of antiprotons (~$50 \times 10^{10}$) in an equilibrium state, i.e., constant distributions, is carried out. First, 5 % of the beam is scraped off in one direction and both the scraper position and the Schottky "emittance" are recorded. Then, the remainder of the beam is scraped away to find the "extinction point" at which the scraper position is also recorded. Assuming that the beta-functions at the scraper and Schottky detectors are known, the scraper travel between the 95 % position and the extinction point gives a measurement of the 95 % emittance at the scraper, which is then computed for the location of the Schottky detector. A calibration factor is thus obtained to convert the beam power of the betatron sidebands measured by the Schottky detector into an emittance number. It should be noted that, strictly speaking, this procedure assumes that the two transverse degrees of freedom are completely uncoupled. An up to ~20 % correction (decrease, i.e., the procedure described *overestimate* the emittance of the beam) needs to be applied when the horizontal and vertical directions are fully coupled. In the Recycler, the coupling is kept to a minimum but cannot be completely eliminated.

In this study, we also used alternate measurements of the transverse and longitudinal emittances. The transverse emittance was measured with the horizontal flying wire, which profile is fitted with a Gaussian function. Note that the flying wire emittance was always lower than the Schottky's by at least a factor of 1.2 (likely a calibration issue), and the ratio was increasing by up to a factor of 2 when the beam was deeply cooled by the electron beam, indicating long non-Gaussian tails.

The longitudinal emittance was calculated with the tomography procedure applied to the longitudinal density profile, acquired with a resistive wall monitor for a fixed measured RF voltage waveform. The tomography approach gave the same qualitative results as the calculation obtained from the Schottky signal for not-too-deeply cooled bunches contained between rectangular barriers. This alternate procedure leads to an even larger stability threshold difference between the two RF configurations described above: for the standard bucket, $D_{95\%} = 10.9$, while $D_{95\%} = 3.8$ for the bucket with barrier height reduced by a factor of 2.

The beam stability was also studied for the beam in the 2.5 MHz RF structure, which mimicked the final stage of the extraction but with significantly stronger electron cooling. Out of four 2.5 MHz bunches, 3 (trailing) bunches went unstable, and their intensity dropped evenly. The oscilloscope traces showed large oscillations of the second bunch, but no oscillations on the others, even at the end of 32 ms recording period. While this structure is clearly far from the coasting beam model considered in Sect. 5.3.1, the threshold density calculated with the flying wire emittance and tomography, $D_{95\%} = 7.2$ (average for the four bunches) was similar to the number found for the long rectangular bunches.

### 5.3.5 *Discussion of the Observations*

The observations did not reveal contradictions with the model presented above. In fact, all the quantitative and qualitative features predicted by the model are in agreement with the observations within their accuracy. Without a damper, the instability occurs at the lowest betatron sideband; with the damper, it happens right outside of the damper bandwidth.

In the measurements with the dampers, the value predicted by Eq. (5.45) for the threshold phase density falls into the scatter of experimental observations. Note that in the case of the 70 MHz damper, the logarithm of Eq. (5.45) is large, ~10. The range of the bunch length and transverse emittance variations in the instability studies results in changes of the logarithm by less than 1.5. Correspondingly, the instability threshold predicted by Eq. (5.45) changes also by less than 15 %, i.e., it is almost a constant at a given chromaticity and damper parameters. The large scatter of $D_{95\%}$ observed in the experiments was attributed primarily to the variations of the tail distribution. In addition, the threshold is clearly affected by the finite height of the longitudinal barriers.

Several features such as a slow non-exponential growth of the oscillations and seconds-long times beam losses were originally unexpected. However, a classical exponential growth of an instability describes the behavior of a system sufficiently above the threshold, while in all our experiments, the beam was slowly reaching the threshold density as it was being cooled. Strictly speaking, the instability growth rate at the exact threshold is zero. Then, in this case, it is determined not only by the impedance but also by such factors as beam cooling, synchrotron motion, and all sorts of diffusion for the resonant particles. That is why for that gradual approach of the threshold, the emerging instability can be orders of magnitude slower than the pure impedance-related growth.

### 5.3.6 *Operational Implications*

The studies confirmed that the beam configuration most prone to become unstable is the mined bucket. To avoid instabilities caused by overcooling the antiprotons, the electron beam current used in operation was limited to 100 mA, and the offset between the beam centers in the cooling section, which is a manipulation used to reduce the cooling rate, was adjusted in order to stay far from an instability. In addition, we eliminated the step during the preparation of the bunches for extraction that originally separated the portion of antiprotons with the largest momentum offsets (the so-called mining [34]). While no dedicated studies were performed, operationally it allowed applying stronger electron cooling, which led to the highest phase density of extracted beams at the end of Run II.

### 5.3.7 Note About the Main Injector

The beam extracted from the Recycler is transferred into an identical 2.5 MHz structure in the main injector (MI). Because both machines have similar lattices—hence the beam brightness does not change significantly during the transfer—and transverse dampers were not used at this stage, one may have expected the development of a transverse instability in MI as well. However, no instability-related antiproton beam loss has ever been observed. The reason is that the MI chromaticity was set to a large value, $-18$, while the measured chromaticity in the Recycler was $-2$ (horizontal)/$-4$ (vertical). Operation of MI at a lower chromaticity, $-12$, resulted in strong horizontal oscillations ([35]) but still not in a beam loss. Note that in the main injector, the beam spends less than 3 s at the injection energy, and the beam lifetime reduction due to high chromaticity is not an issue. Attempts to operate with a similarly large chromaticity in the Recycler were unsuccessful because of the deterioration of the beam lifetime, and in operation, the chromaticity is set to a much smaller value than for MI.

### 5.3.8 Conclusions

The transverse instability of the antiproton beam in the Recycler was the final limiting factor to the brightness of the extracted beams that could be achieved. Nevertheless, the transverse dampers in conjunction with electron cooling permitted to increase the beam brightness by an order of magnitude.

Qualitative features of the measured instances of the instability fit reasonably well the model developed for a coasting beam. The onset of the instability is determined by the threshold phase density, which value is in agreement with the model within the scatter of experimental data and the precision to which this theoretical threshold can be calculated. The scatter in the data is likely related to variations in the distribution of the tails particles, which determine Landau damping. In particular, lowering the potential depth of the barrier bucket effectively excludes part of the longitudinal tails from damping and may decrease the threshold density by a factor of 2.

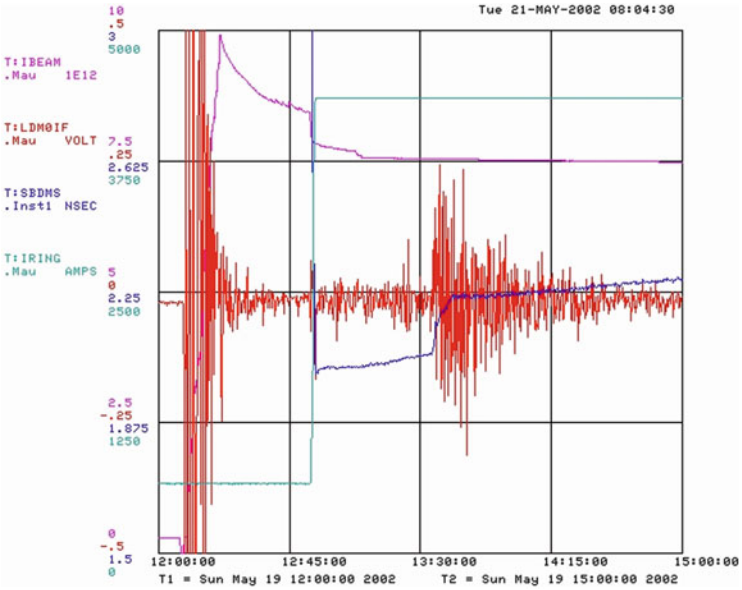


**Fig. 5.11** The beam blows up longitudinally (*blue line*, T:SBDMS, the rms bunch length average for all bunches) at about 13:40 h during the store which started at about 13:00 h. We see that when it blows up the phase signal of the bunch oscillates w.r.t. RF (T:LDM0IF). Plotted also are the Tevatron average beam current T:IBEAM and the Tevatron magnet bus current T:IRING [11]

## 5.4 The Tevatron Wideband Longitudinal Coupled Bunch Mode Dampers

When Run II began in its first year, the high current stored in the Tevatron caused unforeseen problems in the beam dynamics. These needed to be fixed before higher luminosities could be achieved. One of the problems that started to appear at the beginning of 2002 was the rapid blowup of the longitudinal beam size during a store (see Fig. 5.11). Although these blowups did not appear in every store, they seem to be weakly correlated with beam current. There were conjectures that coupled bunch mode instabilities that arose from coupling to the higher-order parasitic modes of the RF cavities were the cause of the instabilities. As the frequency of these higher modes moves as a function of temperature, the coupled bunch modes can be stable or unstable depending on where and how the higher-order parasitic modes line up. Table 5.3 shows 11 stores in the month of May where about 2/3 of the stores were unstable.

The first attempts at controlling this blowup with mode 0 dampers ended in failure. This showed us that the instability may be a longitudinal head-tail or higher-order coupled bunch mode. At the time, we did not have the instrumentation to distinguish between the two types. After much discussion, it was decided that the best course of action was to build a wideband longitudinal damper system which would take care of the coupled bunch mode instabilities. At first glance, the idea of

**Table 5.3** Comparison of different stores

| Store | Date | Num. protons | Bunch length before blowup (ns) | Bunch length after blowup (ns) | Time before blowup (min) | Bunch lengthening time before blowup (h) | 1/e time after blowup (h) | Comments |
|---|---|---|---|---|---|---|---|---|
| 1302 | 8 May 2002 | 1.7e11 | 2.0 | 2.3 | 60 | 42 | 67 | |
| 1305 | 9 May 2002 | 1.67e11 | 2.0 | 2.3 | 6 | 12 | 43 | |
| 1307 | 10 May 2002 | 1.79e11 | 2.0 | | | 53 | | No blowup |
| 1309 | 11 May 2002 | 1.71e11 | 2.0 | | | 42 | | No blowup |
| 1313 | 12 May 2002 | 1.76e11 | 2.0 | | | 40 | | No blowup |
| 1329 | 16 May 2002 | 1.76e11 | 1.9 | 2.2 | 3 | No data | 77 | |
| 1332 | 17 May 2002 | 1.78e11 | 1.9 | 2.4 | 6 | 9 | 83 | |
| 1333 | 18 May 2002 | 1.81e11 | 2.1 | | | 50 | | No blowup |
| 1335 | 19 May 2002 | 1.77e11 | 2.0 | 2.2 | 39 | 40 | 59 | |
| 1337 | 20 May 2002 | 1.83e11 | 2.0 | 2.2 | 16 | 19 | 56 | |
| 1340 | 21 May 2002 | 1.94e11 | 2.0 | 2.6 | 2 | No data | No data | |

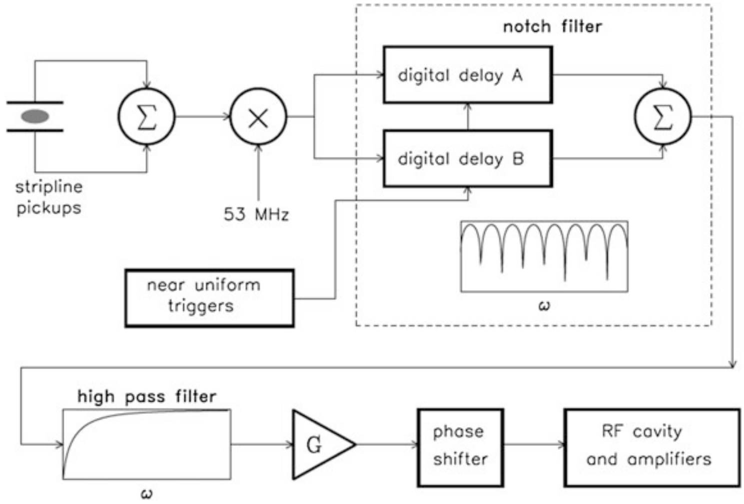


**Fig. 5.12** The block diagram of the longitudinal dampers [11]

using the RF cavity themselves as the source of longitudinal kicks on the beam seems to be difficult. This is because each of the four proton RF cavities has a high-quality factor $Q$ ($\approx 10^4$) near its resonance, and thus, its impedance falls off rapidly away from it. Therefore, the amplitude and phase response is not flat at all synchrotron sideband pairs, and the response of the dampers for the mode 1 coupled bunch mode will be an order of magnitude greater than the higher-order coupled bunch modes. It would be impossible to keep the feedback stable for mode 1 and still have useful gain at the higher-order modes. The solution to this problem is to build an equalizer that lifts up the impedance so that it looks constant away from the resonance. Besides the equalizer, the damper also needs a notch filter that suppresses the revolution harmonics (otherwise these harmonics will limit the gain of the loop) and differentiates in time the synchrotron sidebands. Lastly, we also have to time in the system so that the error signal of bunch $n$ is applied exactly one turn later to kick bunch $n$.

The block diagram of the damper system [11] is shown in Fig. 5.12. The damper system starts at the stripline pickups which sum the beam signals at the two plates to produce a signal that is proportional to the longitudinal position of the beam. This signal is then down converted with the Tevatron RF to produce a phase error (or quadrature) signal w.r.t. it. The error signal is then processed with electronics that perform the following:

(a) Equalize the impedance of the RF cavity
(b) Suppress the revolution harmonics and differentiate the synchrotron sidebands around the revolution lines
(c) One turn delay so that when the dampers pick up the signal of bunch 1, it will kick bunch 1 one turn later

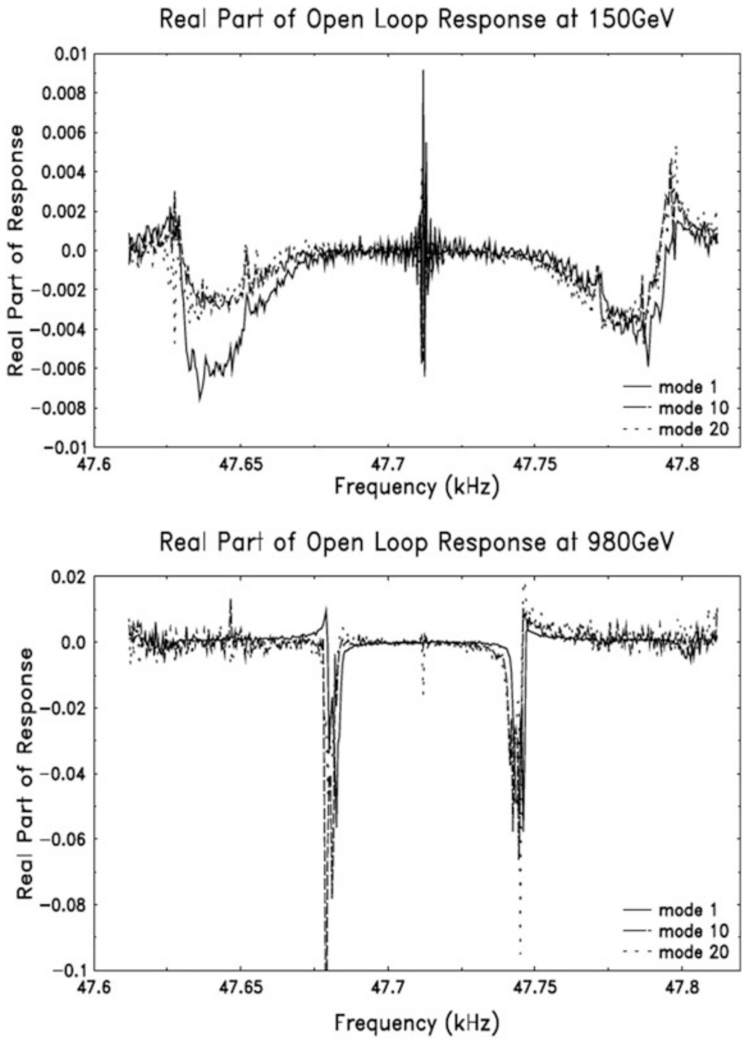


**Fig. 5.13** These graphs show the real part of the open-loop response of modes 1, 10, and 20 at 150 and 980 GeV. We have superimposed all the three graphs on top of each other by shifting the frequency of mode 10 by $-10f_0$ and mode 20 by $-20f_0$ [11]

To accomplish (a), we have a high-pass filter (HPF) that equalizes the RF cavity impedance, and for (b) and (c), we have digital notch filters that provide tracking delay and a notch at every revolution harmonic.

The real part of the open-loop transfer measurement of the setup at 150 and 980 GeV is shown in Fig. 5.13. For damping, it is necessary that the real part of the response at $\pm f_s$ be symmetric about the revolution harmonic and negative. A sampling of the open-loop transfer functions of modes 1, 10, and 20 presented in this figure shows that the dampers are phased correctly. Note that the edges of the

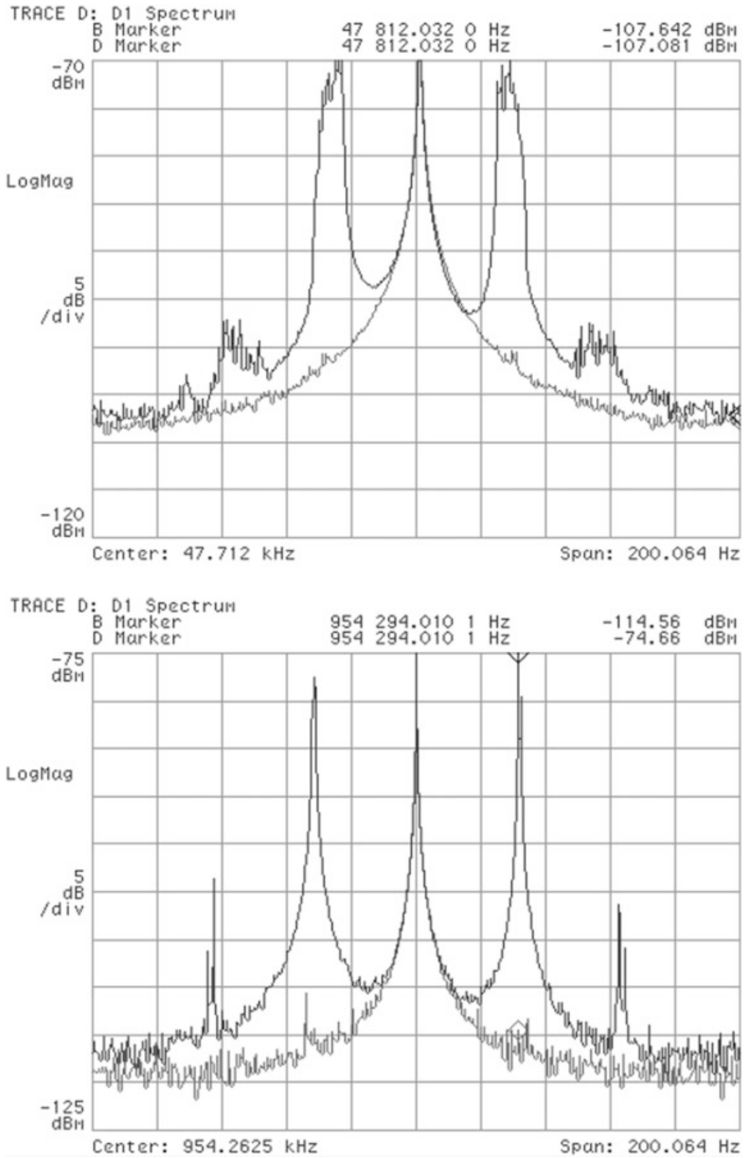


**Fig. 5.14** The beam spectra at 980 GeV; top - before the measurement the loop was closed, then the beam was excited by anti-damping; bottom - the damping was turned on resulting in the synchrotron lines of modes 1 and 20 being damped [11]

response are positive rather than negative. This limits the amount of gain that can be set in the damper system.

To test whether the dampers indeed work, we can excite the beam at 980 GeV by switching the sign of the gain. This is a good sign because we can actually excite the beam which means that there is sufficient gain in the loop. When we switch the sign of the gain back to damping, we find that the excitation can be damped. The results of these actions are shown in Fig. 5.14. Although the dampers do perform their job, we find that damping takes 2–3 min in these examples.

After installing the dampers, the problem of sudden beam size growth during a store is rarely observed. To prove to ourselves that the dampers definitely stopped the problem, we deliberately turned the dampers off for one store. In this store the beam blew up longitudinally as before. This conclusively showed us that the longitudinal dampers solved the problem. However, the underlying cause of the blowup is still not understood. There are speculations that higher-order parasitic modes in the RF cavity, phase noise from microphonics, etc. are the source of these blowups. However, operationally, the dampers were a success.

## References


1. P.M. Ivanov et al., in *Proceedings of the IEEE PAC'2003*, Portland, OR (2003), p. 3062
2. C.-Y. Tan, J. Steimel, *Fermilab Preprint FERMILAB-TM-2204*, 2003
3. P.M. Ivanov et al., in *Proceedings of IEEE PAC'2005*, Knoxville, TN (2005), p. 2756.
4. V. Lebedev, A. Burov, W. Pellico, X. Yang, *Prepint FERMILAB-CONF-06-205-AD*, 2006
5. A. Burov, V. Lebedev, Phys. Rev. ST Accel. Beams **10**, 054202 (2007)
6. L.R. Prost et al., *Transverse Instabilities in the FERMILAB Recycler*, arXiv:1201.4168 (2012)
7. A. Burov, V. Lebedev, Phys. Rev. ST Accel. Beams **12**, 034201 (2009)
8. A. Burov, V. Lebedev, AIP Conf. Proc. **773**, 350 (2005)
9. R. Moore et al., in *Proceedings of the IEEE PAC'2003*, Portland, OR, p. 1751
10. W. Guo et al., FERMILAB-TM-2203 (2003)
11. C.-Y. Tan, J. Steimel, *FERMILAB-TM-2184*, 2002
12. S.C. Snowdon, *Fermilab TM-277*, 1970
13. A. Ruggiero, Fermilab FN-220 0402 (1971)
14. R. Gluckstern, *Fermilab TM-1374*, 1985
15. K.Y. Ng, *Fermilab FN-0744*, 2004
16. A. Macridin, P. Spentzouris, J. Amundson, L. Spentzouris, D. McCarron, Phys. Rev. ST Accel. Beams **14**, 061003 (2011)
17. A. Burov, V. Lebedev, *FERMILAB-CONF-02-101-T*, 2002
18. A. Burov, V. Lebedev, *FERMILAB-CONF-02-100-T*, 2002
19. A.W. Chao, *Physics of Collective Beam Instabilities in High Energy Accelerators* (Wiley, New York, 1993)
20. A. Burov, *LHC Project Note 353*, 2004
21. J. Crisp, *Fermilab-TM-2145*, 2001
22. K. Yokoya, H. Koiso, Part. Accel. **27**, 181 (1990)
23. R. Gluckstern, J. van Zeijts, B. Zotter, Phys. Rev. E **47**, 656–663 (1993)
24. L.R. Prost et al., in *Status of Antiproton Accumulation and Cooling at Fermilab's Recycler*. Proceedings of the COOL'09, Lanzhou (2009) MOM1MCIO01
25. A. Burov, V. Lebedev, PRSTAB **12**, 034201 (2009)
26. L.R. Prost et al., in *Transverse Instability of the Antiproton Beam in the Recycler Ring*. Proceedings of the PAC'11, New York (2011)
27. A. Burov, V. Lebedev, AIP Conf. Proc. **773**, 350–354 (2005)
28. V. Balbekov, PRSTAB **9**, 064401 (2006)
29. A. Burov, Phys. Rev. ST Accel. Beams **12**, 044202 (2009)

30. L. Michelotti, Phys. Rev. ST Accel. Beams **6**, 024001 (2003)
31. A. Burov, in *Instabilities and Phase Space Tomography in RR*. Fermilab Internal Report beams-doc-3641 (2010)
32. N. Eddy, J.L. Crisp, M. Hu, AIP Conf. Proc. **868**, 293–297 (2006)
33. N. Eddy, J.L. Crisp, M. Hu, in *Measurements and Analysis of Beam Transfer Functions in the Fermilab Recycler Ring Using the Transverse Digital Damper System*, Proceedings of the EPAC'08, Genoa (2008)
34. C.M. Bhat, Phys. Lett. A **330**, 481–486 (2004)
35. M.J. Yang, J. Zagel, *Fermilab Internal Note* beam-doc-3649 (2010), http://beamdocs.fnal.gov/AD-public/DocDB/ShowDocument?docid=3649